Inorganic Chemistry

Article

pubs.acs.org/IC

Classical Characterization Techniques to Reveal the Structural Model of Nanocomposites with Bimetallic Monolayers of Porphyrins

Mariana Hamer[§] and Irene N. Rezzano*[,§]

[§]IQUIFIB-CONICET, Faculty of Pharmacy and Biochemistry, University of Buenos Aires, Junin 956, CP 1113 Buenos Aires, Argentina

ABSTRACT: Nanocomposites with bimetallic monolayers of porphyrins were prepared. The well-ordered metalloporphyrin monolayers covalently linked to the gold surface produce an important increase of the B band (~400 nm) shifted 20 nm relative to that of the related high-spin iron(III) complexes in solution. The position of the B band in the bimetallic architectures is highly dependent on the relative amount of the two porphyrins, showing the most significant shift for the SiO_2/APTES/AuNp/Fe-TPyP&M-TPyP (1:1) (30 nm, M = Ni(II) or Cu(II)). Resonance Raman based on the oxidation state marker bands (1553, 1354, and 390 cm^{-1}) indicates that Fe-TPyP attached on gold nanoparticles adopts a low-spin Fe(II) conformation, which changes to Fe(II) intermediate spin or a low-spin Fe(III) in the presence of Cu-TPyP or Ni-TPyP. Surface-enhanced Raman scattering studies confirmed the hypothesis. MALDI-TOF analysis of the composites on gold nanoparticles was very useful in the detection of oxygenated forms of the metal complexes.

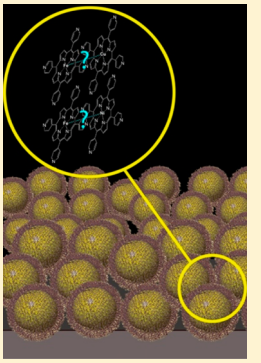

INTRODUCTION

A large number of metal organic compounds, especially high valence metal complexes formed as the result of redox reactions, has been synthesized and characterized in the few last years.[1−3] Most of these studies were carried out with the aim of getting a deeper insight into the active site of metalloenzymes to understand the reaction mechanisms of many metabolic processes.[4−6] An interesting aspect to evaluate is the difference between the formal oxidation number and the experimental oxidation state of the metal in many biological systems. Various radicals are formed at a proximal position of the metal center due to the presence of ligands that do not necessarily possess a closed-shell configuration (noninnocent ligands).[7,8] Metalloporphyrins belong to this class of ligands, playing a critical role in biological systems where they participate as the redox center of many enzymes. The reduction of molecular oxygen occurs through a different mechanism ruled by the metal and/or axial ligands involved.[9] As an example, we can mention that the cytochrome P450 provides three electrons from the oxidation of Fe (II) to Fe (IV) and from the porphyrin ring that forms a π-cationic radical.[10] However, other enzymes contain bimetallic catalytic centers, such as the soluble di-iron methane monooxygenase (sMMO) and dicopper tyrosinase, in which the existence of Fe−Fe and Cu−Cu interactions plays a basic role in the enzymatic activity.

The heterobimetallic centers also have a great prominence in nature, such as the heme/copper combination in cytochrome c oxidases to the efficient reduction of O_2 to H_2O and the Ni−Fe couple that catalyzes the conversion of protons to hydrogen with soluble [NiFe] hydrogenases. Although both metals are essential for catalysis, their individual roles remain uncertain, and for this reason, the study of the oxidation state, geometry, and coordination number is especially attractive. Undoubtedly, the redox active center defines the functionality of these enzymes and has been intensively studied by a variety of spectroscopic methods including UV−visible/near-IR, CD and MCD, EPR and ENDOR, vibrational mid-IR, and Raman.[11]

Research in nanostructured materials has increased over the few last years because they have optical and electrical properties that differ significantly from bulk materials due to the increased relative surface area and quantum effects.[12,13] The functionalization of metal nanoparticles with redox and optically active compounds modifies the electron density of the metallic nanoparticles with an immediate effect in both the conductivity of the organic moiety and surface plasmon of the nanoparticles.[14] This behavior has optical and electronic implications in terms of sensitivity, allows characterization of the resulting structures, and evaluates their functional performance. The arrangements of metalloporphyrins can be studied by absorption spectroscopy on supported gold nanoparticles (AuNps).[15,16] The absorption band of mono- and bimetallic composites of porphyrin and AuNps deposited onto transparent substrates resulted in a significant increase in the porphyrin B absorption band at 412 nm.[17] Furthermore, we observed the steady growth of this absorption band with growing concentrations of hydrogen peroxide added to the heterobimetallic nanocomposites, and the Kapp obtained was very close to the value reported for the peroxidase enzyme.[17] Moreover, the presence of Fe-TPyP produced changes in the geometry of the adsorbed Cu-TPyP porphyrins, resulting in the special accommodation of the porphyrinic rings in the Fe-TPyP&Cu-TPyP composite, which could be the reason for the differential tendency to include H_2O_2 from the observed in

Received: May 9, 2016

DOI: 10.1021/acs.inorgchem.6b01136
Inorg. Chem. XXXX, XXX, XXX−XXX

Scheme 1. (A) Structure of 5,10,15,20-Tetra(4-pyridyl)-21*H*,23*H*-porphine metallocomplexes (M-TPyP) and (B) Schematic Representation of the Assembly Procedure onto the SiO_2 Surface Showing the APTES Self-Assembled Monolayer and Adsorption of AuNps and M-TPyP

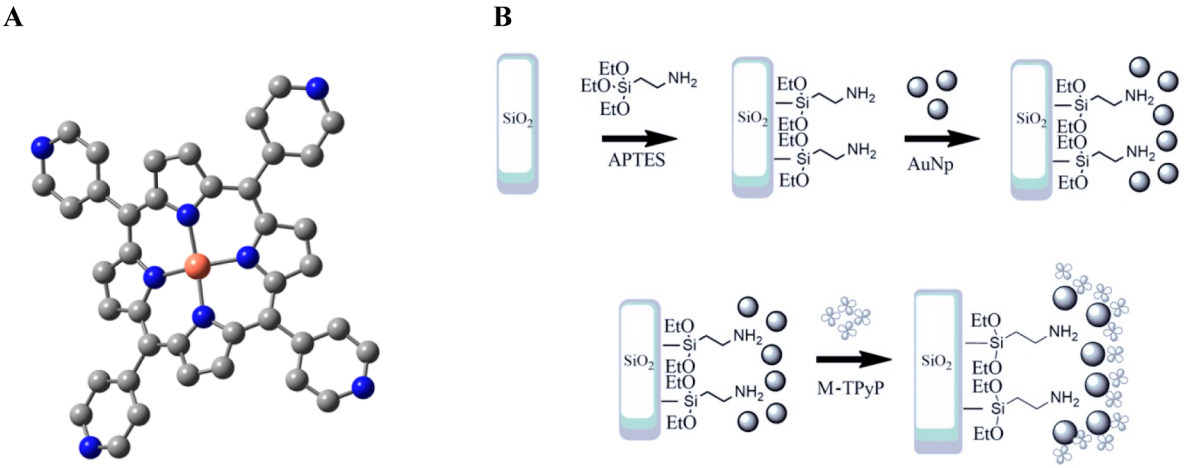

solution. These results encouraged us to employ conventional characterization techniques to understand the structural model and functional behavior of nanocomposites with bimetallic monolayers of porphyrins.

Here, we report the use of resonance Raman scattering (SERR) and surface-enhanced Raman scattering (SERS) to obtain information about the structure, orientation, and spin state of molecular compounds adsorbed on metallic nanostructures.[18,19] The UV−vis spectra also resulted conclusive to the analysis of the nanocomposites. On the other hand, matrix-assisted laser desorption/ionization mass spectrometry (MALDI/MS) was applied in the present work to complement the structural information on the nanomaterials because AuNps, similar to other nanostructures, have been reported as ionization elements for small molecules.[20]

■ EXPERIMENTAL SECTION

Reagents. Analytical grade gold(III) chloride trihydrate salt (Aldrich) and sodium citrate were used as supplied. Metallocomplexes (M-TPyP) of 5,10,15,20-tetra(4-pyridyl)-21*H*,23*H*-porphine [Fe(III), Cu(II), and Ni(II)] were prepared according to standard procedure.[21] 3-Amino-propyl-triethoxysilane (APTES) was purchased from Fluka. All other reagents were obtained from Merck and used as received. Water was deionized and filtered using a Millipore water purification system (18 MΩ).

Apparatus. An Evolution Array UV−visible spectrophotometer (Thermo Scientific) and a quartz crystal cell were used to obtain the UV spectra. Raman scattering spectra were collected on a Renishaw in-Via Reflex confocal microspectrometer equipped with a CCD detector of 1024 × 256 pixels, a holographic grating of 2400 grooves/mm, and a 50 mW Ar laser (514 and 690 nm wavelength) as the excitation source. Spectra were measured in the 100−1600 cm^{-1} Raman shift region at 1 cm^{-1} spectral resolution. Measurements were carried out in conditions of high confocality (3 pixels of the CCD detector and 20 μm slit width) through a 100× Leica metallurgical objective (numerical aperture of 0.9), which limits the diameter of the laser beam to about 1 μm.

The mass spectrometric analysis was performed using a low-resolution matrix-assisted laser desorption ionization, time-of-flight mass spectral technique with MALDI-TOF equipment Plus ABSCIEX 4800. Molecular species were detected in the mass spectra as clusters of peaks because of the isotopic composition. Therefore, to simplify their assignments, m/z values reported in the spectra and the text refer to the ion containing the most abundant isotope of each element.

The scanning electron micrographs of the modified surfaces were obtained using a Zeiss DSM982 GEMINI SEM instrument with a field emission gun (FEG) operated at 3 kV. The nanoparticle size was determined using ImageJ, an open source Java image processing program inspired by NIH Image.

Synthesis of AuNps. AuNps were synthesized by a modification of the Turkevich method.[22] In brief, 4.5 mg of gold(III) chloride trihydrate ($HAuCl_4·3H_2O$) was dissolved in 45 mL of Milli-Q water, and 10 mL of this solution was brought to boil in a round-bottom flask under stirring. A 1.6 mL portion of a 1% sodium citrate solution was added and stirred. Boiling was maintained for 20 min, after which the heat was removed and stirring was continued for 15 min. Then, 8 mL of the nanoparticle suspension was centrifuged in 1.5 mL Eppendorf tubes at 7000 rpm (4.500g) for 45 min to remove excess reducer; the supernatant was removed, and the remaining AuNps were redispersed.

The same procedure was applied to obtain bigger AuNps, the portion of sodium citrate was changed to 1 mL.

Surface Modification. Before use, SiO_2 plates were cleaned with "piranha" solution (H_2SO_4:H_2O_2, 3:1). Piranha solution must be prepared with great precaution in adding hydrogen peroxide to the sulfuric acid. The mixing is extremely exothermic and, if it is made rapidly, may release a great amount of corrosive fumes. Surfaces must also be reasonably clean and completely free of organic solvents to be immersed into this solution because a large amount of organic material can cause violent bubbling.

The clean glasses were then immersed into a 10% (v/v) solution of APTES in ethanol for 6 h, rinsed extensively with ethanol, and dried in a N_2 stream and a 60 °C oven for 6 h. The functionalized surfaces were placed into the AuNp suspension for 12 h to form a monolayer, copiously rinsed with H_2O, and immersed (12 h) in a M-TPyP solution at pH 2. The samples were soaked in water and kept at room temperature until use.

For UV−vis measurements, the modified SiO_2 plates (1 × 2 cm) were introduced in the quartz cuvette filled with water. For the MALDI-TOF study, the nanocomposites were frictionally removed from the SiO_2 plates, deposited on the MALDI target plate, and analyzed without using a matrix.

Determination of the Amount of Porphyrin Deposited onto AuNps. The amount of adsorbed M-TPyP on the AuNp surface was estimated by measuring the absorbance of the nanocomposite at 430 nm after baseline correction. The averages of the two highest absorption responses were 0.067 and 0.065 for Cu-TPyP and Fe-TPyP&Cu-TPyP 1:3, respectively. Then, using the Lambert−Beer law $A = \varepsilon \times L \times [\text{M-TPyP}]$, where $\varepsilon = 1.8 \times 10^5$ M^{-1} cm^{-1}; L = thickness of the porphyrin monolayer/porphyrin diameter, 2×10^{-7} cm; and [M-TPyP] = M-TPyP molar concentration. The procedure was

DOI: 10.1021/acs.inorgchem.6b01136
Inorg. Chem. XXXX, XXX, XXX−XXX

repeated three times for each nanocomposite, and the average value was expressed.

The calculated [M-TPyP] was 3.4 M. So, for a volume of 1000 cm^3 where the height is the thickness of the monolayer (equivalent to the optical space), the amount of M-TPyP per cm^2 was estimated to be 6.4 $\times 10^{-10}$ mol/cm^2. This calculation was performed in triplicate, and the reproducibility was checked.

RESULTS AND DISCUSSION

Surface Modification. The AuNps were immobilized on a transparent substrate by attachment to the APTES-coated glass

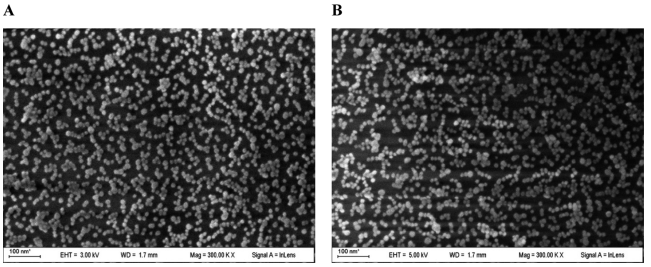

Figure 1. SEM image magnification at 300 K× of the SiO_2/APTES/AuNp (A) and SiO_2/APTES/AuNp/M-TPyP (B) surfaces.

(SiO_2) surface: SiO_2/APTES/AuNp. Then, this array was modified with metalloporphyrins (M-TPyP) by the direct binding of the porphyrin ring to the nanoparticles.[23] A monolayer of porphyrins was obtained. The sequence of the modification procedure is shown in Scheme 1B.

SEM images (Figure 1) reveal the morphology and order degree of the nanostructured surface. A dense and uniform distribution of nanoparticles on the glass substrate can be observed with an average particle size of 21 ± 0.5 nm which changed to 23 ± 0.8 nm after being coated with M-TPyP.

The amount of immobilized M-TPyP on the AuNps was determined, and the surface coverage of 6.4 $\times 10^{-10}$ mol cm^{-2} was obtained, which is quite similar to that reported by Karlin et al.[24] for a monolayer on a planar surface (1.5 $\times 10^{-10}$ mol cm^{-2}). Therefore, the present design can be considered for the M-TPyP in the monolayer level. Later results obtained by MALDI-TOF experiments confirmed this idea.

Table 1. Maximum Wavelength of the Soret band in Each Nanocomposite

	λ_{max} (nm)
Fe-TPyP	430
Ni-TPyP	420
Cu-TPyP	420
Fe-TPyP&Ni-TPyP (1:1)	440
Fe-TPyP&Cu-TPyP (1:1)	440
Ni-TPyP&Cu-TPyP (1:1)	420

UV−Vis. The UV−visible spectra of the nanocomposites show an absorbance maximum at 532 nm for AuNps (Figure 2 black), which corresponds to a particle size of 20 nm[25,26] as observed by SEM. In contrast, the deposit of porphyrin onto the gold surface produces a more intense and wider plasmon band, which also shifted to 560 nm.[27]

As it is known, the optical absorption spectra of porphyrins show two significant absorption bands named B and Q, corresponding to a high electronic transition at about 400 nm and a weak transition at about 550 nm, respectively.[27] The covalent linkage of the porphyrin to the gold surface produces an orbital overlap of the molecular π system ($\theta \sim 0$), resulting in a remarkable increase in the B band that can be explained regarding photon-plasmon conversion, whereas the gold plasmon signal hides the band at 500 nm.[28]

The monolayer of Fe-TPyP on AuNp surface exhibits a peak at 430 nm (Figure 2, red), which is red-shifted by 20 nm relative to that of the related high-spin iron(III) complexes in solution (400−415 nm region).[24] This shift could be attributed to the electronic interaction between Fe(III) and the gold surface,[29,30] which changes the oxidation state of the iron to Fe(II) (λ_{max} 440).[31] The Soret band position of Cu-TPyP and Ni-TPyP in the composites was less affected by the immobilization. Accordingly, a band at 420 nm was observed for SiO_2/APTES/AuNp/Cu-TPyP and for SiO_2/APTES/AuNp/Ni-TPyP. However, the combination of Fe-TPyP with either Cu-TPyP or Ni-TPyP produced a bathochromic shift of the Soret band, which is highly dependent on the relative amount of the two different porphyrins. Therefore, to gain insight into the stoichiometry of the process, we obtained the

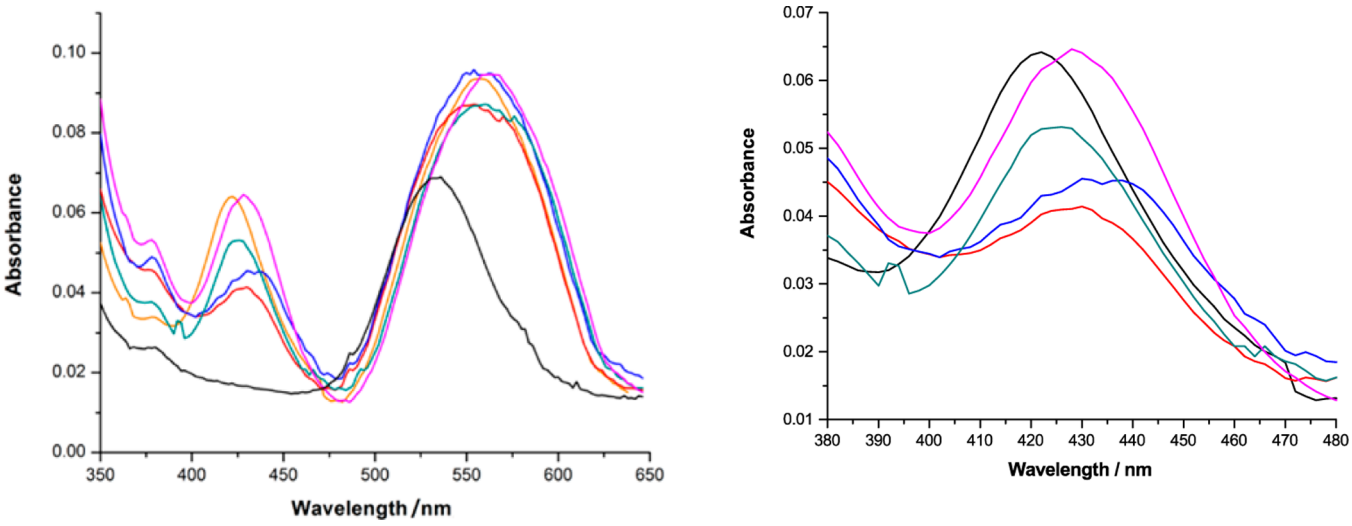

Figure 2. (A) Absorbance spectra of SiO_2/APTES/AuNp (black) and SiO_2/APTES/AuNp/M-TPyP: Cu-TPyP (orange), Fe-TPyP (red), Fe-TPyP&Cu-TPyP 1:3 (purple), Fe-TPyP&Cu-TPyP 1:1 (blue), and Fe-TPyP&Cu-TPyP 3:1 (green). (B) Zoom between 380 and 480 nm.

DOI: 10.1021/acs.inorgchem.6b01136
Inorg. Chem. XXXX, XXX, XXX−XXX

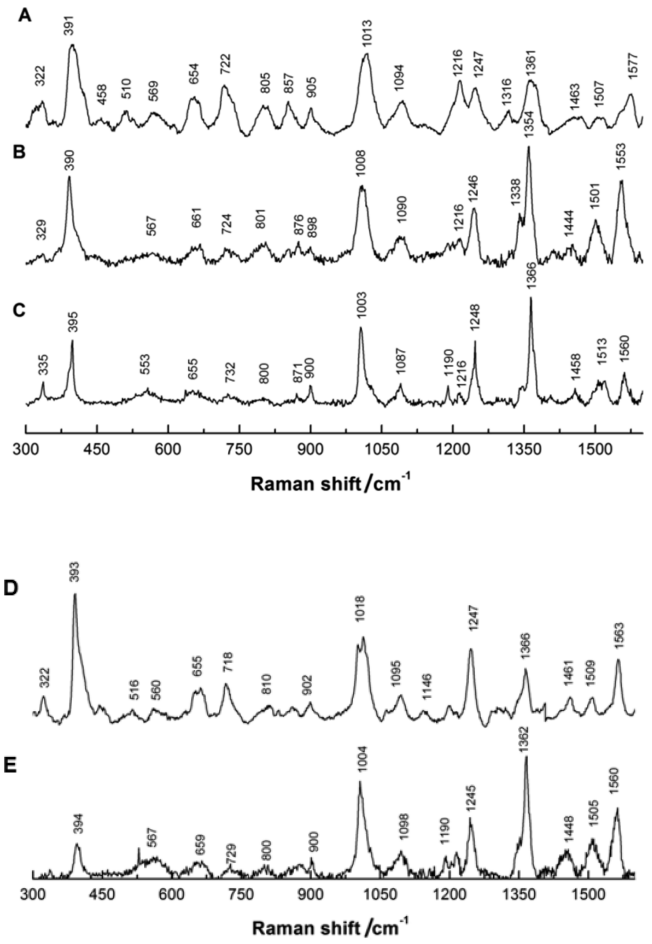

Figure 3. SERRS spectra of SiO_2/APTES/AuNp/M-TPyP: (A) Ni-TPyP, (B) Fe-TPyP, (C) Cu-TPyP, (D) Ni-TPyP&Fe-TPyP, and (E) Cu-TPyP&Fe-TPyP. Excitation wavelength: 514 nm.

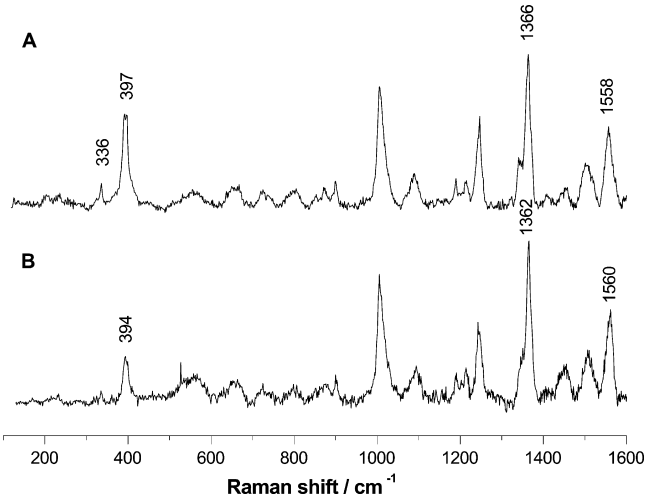

Figure 4. (A) Theoretical and (B) experimental SERRS spectra for SiO_2/APTES/AuNp/Fe-TPyP&Cu-TPyP.

absorption spectra of three bimetallic nanocomposites prepared with various proportions of metalloporphyrin.

Figure 2 shows these results: SiO_2/APTES/AuNp/Fe-TPyP&Cu-TPyP (3:1) (430 nm), SiO_2/APTES/AuNp/Fe-TPyP&Cu-TPyP (1:1) (440 nm), SiO_2/APTES/AuNp/Fe-TPyP&Cu-TPyP (1:3) (425 nm). Interestingly, the more

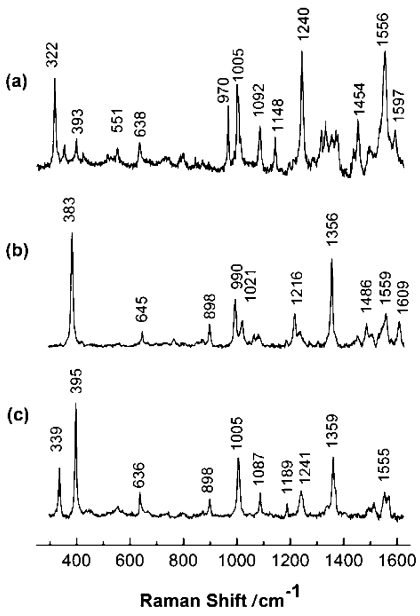

Figure 5. Raman spectra of solid (a) Ni(II)-TPyP, (b) Fe(III)-TPyP-Cl, and (c) Cu(II)-TPyP. Excitation wavelength: 514 nm.

significant shift is observed for the SiO_2/APTES/AuNp/Fe-TPyP&Cu-TPyP (1:1) (440 nm) which is consistent with an internal redox reaction between the Cu-TPyP and Fe-TPyP molecules changing the oxidation state of the iron complex. The highest effect is achieved with a 1:1 stoichiometry.[32]

The composite Ni-TPyP&Fe-TPyP (1:1) also shows a similar bathochromic shift, whereas no change of the Soret band was observed for the combination of Ni-TPyP with Cu-TPyP (Table 1). This effect is due to the overlapping of the electronic transitions of the two metalloporphyrins. Interestingly, it occurs with only the combinations Fe/Cu and Fe/Ni, which produce a high number of mixed-valence heteronuclear complexes. Similar results have been reported for other types of ligands where the orientation of the two metal centers defines the functional behavior.[33]

As it is well-known, the formation of a side-by-side partially $\pi-\pi$ stacked structure of the porphyrin ring (J-aggregates) can cause a red-shift of the Soret band.[34,35] However, in this case, the J-aggregates cannot explain the increase in the intensity of the Soret band in the nanocomposites, and the results of MALDI-TOF, SERRS, and SERS endorse this statement (vide infra).

Resonance Raman Spectroscopy. On the basis of an ideal *D4h* symmetry of the porphyrin, the resonance Raman (RR) active modes can be classified into *A1g*, *A2g*, *B1g*, and *B2g* symmetry modes.[36] The symmetric *A1g* modes dominate at Soret excitation, while excitation via B-term scattering enhances the patterns that are not totally symmetric. Thus, excitation with 514 nm for Raman scattering is also resonant with the surface plasmon mode of the constituent AuNps and Q absorption band of the mono and bimetallic composites. Figure 3 shows the Raman spectra in this double resonance Raman condition (SERRS) for Fe-TPyP, Cu-TPyP, and Ni-TPyP. As it is observed, strong porphyrin skeletal modes and weak metal–ligand vibrations dominated the spectra.

In all of the composites, the intensity of the pyridine bands (~660, 900, 1008, 1200, and 1245 cm^{-1}) increased in comparison with those of the porphyrin ring in the SERRS

DOI: 10.1021/acs.inorgchem.6b01136
Inorg. Chem. XXXX, XXX, XXX–XXX

Table 2. SERS Frequency (cm^{-1}) Assignments for the Nanocomposites[a]

Cu-TPyP	Fe-TPyP	Ni-TPyP	Fe-TPyP&Cu-TPyP (1:1)	Fe-TPyP&Ni-TPyP (1:1)	assignment
335	329	322	334	323	δ porphyrin translation[47]
397	390	391	394	393	γ porphyrin, pyr rotation
		458			ν Ni^{2+}-O
		510		513	δ pyridine
553	567	569	558	566	δ porphyrin and Cu−O stretch[48]
655	661	654		658	δ porphyrin
732	724	722	728	721	δ pyridine
800	795	805	800	803	δ porphyrin
				810	ν Ni^{3+}-O[49]
871	876	857	871	861	δ pyridine
900	898	905	901	900	ν pyridine
1003	1008	1013	1004	1006	ν porphyrin
1087	1090	1094	1098	1093	δ C_β − H
1190			1184	1148	δ pyridine
1216	1216	1216	1216	1201	δ pyridine
1248	1246	1247	1246	1249	δ pyridine
		1316			δ pyridine
1366	1354	1361	1365	1367	ν C_α-N
1458	1444	1463	1450	1457	ν C_α-C_m + ν C_α-C_β ó ν pyridine
1513	1501	1507	1507	1510	ν_{sym} C−C + δ_{asym} porphyrin
1560	1553	1577	1562	1563	ν porphyrin

[a]Assignments: ν, stretching; γ, folding out of the plane; δ, flection. Excitation wavelength: 690 nm.

spectra, which reflects the perpendicular or tilted accommodation of the pyridyl group to the gold surface.[37]

Considering a *D4h* symmetry, Spiro et al.[38] and Lehnert et al.[39] assigned the vibrational spectra of [Fe-(TPP)Cl], and this approach was also accepted for five-coordinate compounds such as [M-(TPP)Cl] (M = Fe, Mn, Co). The same hypothesis can be applied to the analysis of M-TPyP. Thus, the Raman spectra were explored by comparison with (tetraphenylporphyrin) and 5,10,15,20-tetrakis(1-methyl-4-pyridyl)-porphyrin.[40,41]

In the case of the Cu-TPyP-modified surfaces, the typical Cu(II)-porphyrin spectrum was obtained,[42,43] whereas the Fe-TPyP presents significant differences.

In spite of the controversies in the interpretation of RR spectra of highly oxidized metalloporphyrins, a considerable consensus exists on three distinct bands: (I) ∼390, (II) ∼1360, and (III) ∼1560 cm^{-1}.[41] The band at ∼1360 cm^{-1} is one of the most intense polarized bands for either type of porphyrin and probably corresponds approximately to the breathing mode of the pyrrole C−N bonds. This is a well-known "oxidation state marker", shifting from 1370 cm^{-1} in Fe(III) heme groups to 1360 cm^{-1} in Fe(II) complexes with an appreciable spin-state sensitivity. The 390 and 1560 cm^{-1} bands complete the frequency pattern related to the oxidation and spin state of the iron complexes. The frequencies in Figure 3 indicate that the Fe-TPyP on the AuNps surface adopted a Fe(II) low spin conformation (1553, 1354, and 390 cm^{-1}) while results in a Fe(II) intermediate spin or a Fe(III) low-spin conformation when it was codeposited with Cu-TPyP or Ni-TPyP.[40,44] This Fe(III) low-spin electronic configuration described corresponds to a planar geometry of the iron with respect to the atoms of nitrogen of the pyrrole ring,[44] promoting a direct interaction of the iron with the gold surface.[29,30] Furthermore, the incorporation of Cu-TPyP and Ni-TPyP in the SiO_2/APTES/AuNp/Fe-TPyP reduces the intensity of the out-of-phase breathing (Fe−N) mode vibration at 395 cm^{-1} (Figures 3D and E),[39] indicating a change in the conformation of the porphyrin ring.

The experimental SERRS spectra for FeTPyP&CuTPyP was compared with the direct sum of each pondered individual spectra of porphyrins following the hypothesis of the principle of superposition.[43] The high frequency regions seem to be quite similar in both spectra, but differences in the frequency values of the oxidation state marker bands are observed (Figure 4). This nonlinear behavior could be attributed to specific properties of the metallocomplex that are revealed when they interact with each other.[43] In this sense, the noticeable decrease of the band at 390 cm^{-1} suggests a high bimetallic interaction between the iron and copper, as this mode is very sensitive to the structural heterogeneity of the porphyrin macrocycle. Furthermore, the band at 336 cm^{-1}, which is present in the Cu-TPyP nanocomposite, is absent in the experimental spectra of SiO_2/APTES/AuNp/Fe-TPyP&Cu-TPyP.

Similar results are observed for the FeTPyP&NiTPyP system. However, in contrast, the band at 390 cm^{-1} presents an increase of the relative intensity.

On the other hand, the Ni(II) porphyrins are extremely sensitive to the ruffling distortion, as it allows the Ni−N bond to contract to a more energetically favored value.[45] It is interesting to note from a comparison of Figures 3 and 5 that the relative intensity of the peaks at 322 and 393 cm^{-1}, which are associated with pyrrole translation and rotation modes, respectively, are inverted in relation to the normal Raman spectrum, and frequencies of out of plane modes such as 722 cm^{-1} are increased in the composites. It is also worth noticing that the immobilization of the Fe-TPyP on gold nanoparticles produces a fading of the band at 383 cm^{-1} which corresponds to the stretching of Fe−O−Fe and is present in the solid RR spectra.[46] Attachment to the gold surface reduces the formation of μ-oxo bridge of Fe-TPyP due to the direct interaction between the metal center and the gold surface.[29,30]

For SERS analysis, larger gold nanoparticles were used, which presented an absorption band at 700 nm. The results are

DOI: 10.1021/acs.inorgchem.6b01136
Inorg. Chem. XXXX, XXX, XXX−XXX

Table 3. Relative Abundance of the Ions in MALDI-TOF of the Porphyrin/Gold Nanoparticle Composites and Comparison of the Experimental *m/z* with the Calculated Molecular Weight

	MALDI-TOF ion[a]	abundance (%)	weight	assignment
Fe-TPyP	622.15	60	622.25	$C_{40}H_{30}N_8$
	673.26	100	672.14	$C_{40}H_{24}FeN_8$
	825.29	100	824.9	$C_{49}H_{35}FeN_{10}$
	861.3	60	861.28	$C_{52}H_{41}FeN_{10}$
	983.5	28	984.28	$C_{60}H_{40}FeN_{12}$
	969.51	80	970.28	$C_{60}H_{40}FeN_{11}$
Cu-TPyP	622.33	70	622.25	$C_{40}H_{30}N_8$
	680.24	100	679.85	$C_{40}H_{24}CuN_8$
Ni-TPyP	620.31	100	620.25	$C_{40}H_{28}N_8$
	675.22	30	674.99	$C_{40}H_{24}NiN_8$
	692.67	5	697.10	$C_{40}H_{24}NiN_8O$
	711.18	5	713.12	$C_{40}H_{24}NiN_8O_2$
AuNp + Fe-TPyP	622.33	40	622.25	$C_{40}H_{30}N_8$
	673.11	100	672.14	$C_{40}H_{24}FeN_8$
	687.13	25	688.52	$C_{40}H_{24}FeN_8O$
	861.14	18	861.28	$C_{52}H_{41}FeN_{10}$
AuNp + Cu-TPyP	620.2	85	620.3	$C_{40}H_{28}N_8$
	680.15	100	679.85	$C_{40}H_{24}CuN_8$
	760.33	65	759.76	$C_{40}H_{29}Cu_2N_6O$
AuNp + Fe-TPyP + Cu-TPyP	620.19	50	620.3	$C_{40}H_{28}N_8$
	671.98	25	672.14	$C_{40}H_{24}FeN_8$
	680.15	100	679.85	$C_{40}H_{24}CuN_8$
AuNp + Ni-TPyP	620.31	100	620.25	$C_{40}H_{28}N_8$
	675.2	50	674.99	$C_{40}H_{24}NiN_8$
AuNp + Fe-TPyP + Ni-TPyP	620.19	50	620.3	$C_{40}H_{28}N_8$
	671.98	25	672.14	$C_{40}H_{24}FeN_8$
	675.22	30	674.99	$C_{40}H_{24}NiN_8$
AuNp + Ni-TPyP + Cu-TPyP	620.19	50	620.3	$C_{40}H_{28}N_8$
	675.22	30	674.99	$C_{40}H_{24}NiN_8$
	680.15	100	679.85	$C_{40}H_{24}CuN_8$

[a]The experimental peaks present the expected isotopic pattern.[52]

Scheme 2. Schematic Representation of the Fragment $C_{52}H_{41}FeN_{10}$

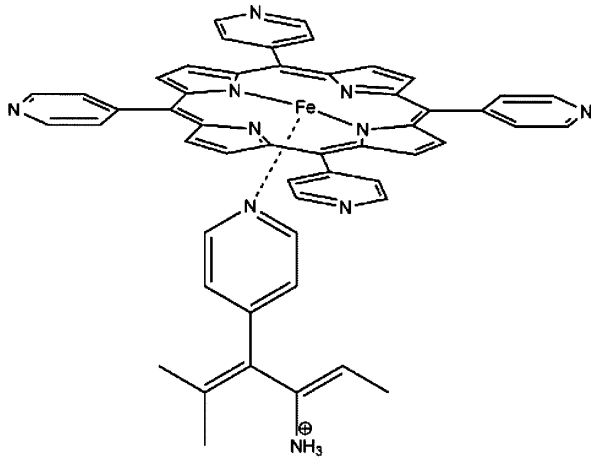

summarized in Table 2. Enhancement of the electric field provided by the surface offers richer information because not only the pyridine bands are increased. In fact, the Ni^{2+}-O band (458 nm) and a Ni^{3+}-O band (810 nm) could be detected in SiO_2/APTES/AuNp/Ni-TPyP and SiO_2/APTES/AuNp/Ni-TPyP&Fe-TPyP, respectively. Additionally, the other oxidation marker bands analyzed by SERRS presented the same pattern behavior.

MALDI-TOF Analysis. Mass spectrometry has been proven to be a very useful tool for analysis in parallel with classical spectroscopic methods. Over the last few years, the nanosized materials, due to their large surface area to volume ratio, provide efficient absorption and transfer of energy to the analyte and function as laser absorption matrixes to provide efficient ionization in the MALDI-TOF MS analysis of small molecules.[50,51] For this reason, MALDI-TOF spectra of free metalloporphyrins were compared with the corresponding nanostructure. The results are summarized in Table 3. It is worth mentioning that the experimental peaks present the expected isotopic pattern.[52]

The MALDI-TOF spectrum of Cu-TPyP shows a dominant intact molecular ion species (100%) and an important peak consistent with the demetalated ion (70%).[52] A similar spectrum was observed for SiO_2/APTES/AuNp/Cu-TPyP. However, it is necessary to emphasize the presence of a new peak of *m/z* 679.85 that can be assigned to an oxycopper−oxygen adduct with Cu_2O stoichiometry.

The MALDI-TOF of Fe-TPyP also exhibits the whole molecular ion species (100%) and the demetalated ion (60%) along with a series of peaks resulting from the fragmentation of the aggregates formed through pyridine axial binding (Scheme 2).[52] On the contrary, the SiO_2/APTES/AuNp/Fe-TPyP shows a cleaner spectrum where only the molecular ion and the demetalated species are present along with *m/z* 688.52 that is ascribed to the highly oxidized Fe(IV) = O metalloporphyrins. Moreover, these results indicate that, when the porphyrin was deposited onto AuNp, the interaction between Fe(III) and pyridines lost strength. Therefore, the formation of multilayers was hindered.

The MALDI-TOF of the bimetallic composite SiO_2/APTES/AuNp/Fe-TPyP&Cu-TPyP also reveals the individual molecular ions and the demetalated TPyP. In this case, it is important to notice that *m/z* 759.76 and 688.52 are absent, probably because the formation of the heteronuclear oxidized form is favored.

The composites containing Ni-TPyP show the same pattern of MALDI-TOF peaks with a high relative abundance of the individual porphyrins and demetalated species. However, the oxygenated species were not observed.

CONCLUSIONS

The present work describes a simple way to study the coordination chemistry of noncovalent bimetallic assemblies of porphyrins. This goal is achieved by coupling between the plasmon (of Au-cluster) and porphyrin's exciton. The FeTPyP on AuNp showed a high tendency to interact with the metallic surface, resulting in a red shift of 20 nm with respect to that of other high-spin iron(III) complexes in solution. This phenomenon was also observed by SERRS and SERS analysis by the study of the spin state marker bands for heme groups. The presence of CuTPyP and NiTPyP in the nanocomposite provoked a change in the Raman frequencies by forcing a different orientation of the porphyrin plane with respect to that of the gold surface. Additionally, lower concentrations of oxygenated species were clearly observed in the MALDI-TOF analysis of the nanocomposites, confirming the coordinative interaction between the metallic centers.

DOI: 10.1021/acs.inorgchem.6b01136
Inorg. Chem. XXXX, XXX, XXX−XXX

A simple principle of bioinorganic chemistry is that the structure and function of large biomolecules can be mimicked using simpler inorganic compounds to model the active sites. In this case, we studied the effect of adding H_2O_2 to the SiO_2/APTES/AuNp/M-TPyP nanocomposite, and the Kapp obtained was very close to the value reported for the peroxidase enzyme.

A number of systems have been synthesized and proposed mainly to study the oxidation, spin state, and coordination number of iron porphyrins, which is especially necessary to fully understand the mechanisms of heme proteins along with the electronic effects of the porphyrin. However, there are still many questions that cannot be answered.

AUTHOR INFORMATION

Corresponding Author

*E-mail: irezzano@ffyb.uba.ar.

Notes

The authors declare no competing financial interest.

ACKNOWLEDGMENTS

Financial support from University of Buenos Aires (Grant UBACyT 2011-14 0915), ANPCyT (Grant PICT 2011-14), and CONICET (Grant PIP 100076) is acknowledged. Dr. J. P. Tomba from INTEMA (CONICET) is gratefully thanked for Raman measurements, Evelyn Hamer is thanked for her help with the English language, and German E. Pieslinger is thanked for his accurate advice.

REFERENCES

(1) Hod, I.; Sampson, M. D.; Deria, P.; Kubiak, C. P.; Farha, O. K.; Hupp, J. T. *ACS Catal.* **2015**, *5*, 6302−6309.

(2) Bougher, C. J.; Liu, S.; Hicks, S. D.; Abu-Omar, M. M. *J. Am. Chem. Soc.* **2015**, *137*, 14481−14487.

(3) Gagnon, N.; Tolman, W. B. *Acc. Chem. Res.* **2015**, *48*, 2126−2131.

(4) Kaim, W. *Inorg. Chem.* **2011**, *50*, 9752−9765.

(5) Rohde, J.-U.; In, J.-H.; Lim, M. H.; Brennessel, W. W.; Bukowski, M. R.; Stubna, A.; Münck, E.; Nam, W.; Que, L. *Science (Washington, DC, U. S.)* **2003**, *299*, 1037−1039.

(6) Tshuva, E. Y.; Lippard, S. J. *Chem. Rev.* **2004**, *104*, 987−1012.

(7) Shimazaki, Y. In *Electrochemistry*; InTech: Rijeka, Croatia, 2013.

(8) Chaudhuri, P.; Verani, C. N.; Bill, E.; Bothe, E.; Weyhermüller, T.; Wieghardt, K. *J. Am. Chem. Soc.* **2001**, *123*, 2213−2223.

(9) Fukuzumi, S.; Yamada, Y.; Karlin, K. D. *Electrochim. Acta* **2012**, *82*, 493−511.

(10) Blusch, L. K. Siamese-Twin Porphyrin and Its Copper and Nickel Complexes: A Non-Innocent Twist. In *Springer Theses*; Springer International Publishing: Cham, 2013.

(11) Kim, E.; Chufán, E. E.; Kamaraj, K.; Karlin, K. D. *Chem. Rev.* **2004**, *104*, 1077−1134.

(12) Nanostructured Materials for Advanced Technological Applications. In *NATO Science for Peace and Security Series B: Physics and Biophysics*; Reithmaier, J. P., Petkov, P., Kulisch, W., Popov, C., Eds.; Springer Netherlands: Dordrecht, the Netherlands, 2009.

(13) Burda, C.; Chen, X.; Narayanan, R.; El-Sayed, M. A. *Chem. Rev.* **2005**, *105*, 1025−1102.

(14) Thomas, K. G.; Kamat, P. V. *Acc. Chem. Res.* **2003**, *36*, 888−898.

(15) Mongwaketsi, N.; Khamlich, S.; Pranaitis, M.; Sahraoui, B.; Khammar, F.; Garab, G.; Sparrow, R.; Maaza, M. *Mater. Chem. Phys.* **2012**, *134*, 646−650.

(16) Shaikh, A. J.; Rabbani, F.; Sherazi, T. A.; Iqbal, Z.; Mir, S.; Shahzad, S. A. *J. Phys. Chem. A* **2015**, *119*, 1108−1116.

(17) Hamer, M.; Carballo, R. R.; Rezzano, I. N. *Sens. Actuators, B* **2011**, *160*, 1282−1287.

(18) Merlen, A.; Gadenne, V.; Romann, J.; Chevallier, V.; Patrone, L.; Valmalette, J. C. *Nanotechnology* **2009**, *20*, 215705.

(19) Baia, M.; Toderas, F.; Baia, L.; Popp, J.; Astilean, S. *Chem. Phys. Lett.* **2006**, *422*, 127−132.

(20) Tseng, M.-C.; Obena, R.; Lu, Y.-W.; Lin, P.-C.; Lin, P.-Y.; Yen, Y.-S.; Lin, J.-T.; Huang, L.-D.; Lu, K.-L.; Lai, L.-L.; Lin, C.-C.; Chen, Y.-J. *J. Am. Soc. Mass Spectrom.* **2010**, *21*, 1930−1939.

(21) Adler, A. D.; Longo, F. R.; Kampas, F.; Kim, J. *J. Inorg. Nucl. Chem.* **1970**, *32*, 2443−2445.

(22) Kimling, J.; Maier, M.; Okenve, B.; Kotaidis, V.; Ballot, H.; Plech, A. *J. Phys. Chem. B* **2006**, *110*, 15700−15707.

(23) Aikens, C. M.; Schatz, G. C. *J. Phys. Chem. A* **2006**, *110*, 13317−13324.

(24) Fox, S.; Nanthakumar, A.; Wei, N.; Murthy, N. N.; Karlin, K. D. *Pure Appl. Chem.* **1993**, *65*, 1.

(25) Link, S.; El-Sayed, M. A. *J. Phys. Chem. B* **1999**, *103*, 4212−4217.

(26) Jain, P. K.; Lee, K. S.; El-Sayed, I. H.; El-Sayed, M. A. *J. Phys. Chem. B* **2006**, *110*, 7238−7248.

(27) Nunes, F. S.; Bonifácio, L. D. S.; Araki, K.; Toma, H. E. *Inorg. Chem.* **2006**, *45*, 94−101.

(28) Zhou, C.; Diers, J. R.; Bocian, D. F. *J. Phys. Chem. B* **1997**, *101*, 9635−9644.

(29) Dees, A.; Jux, N.; Tröppner, O.; Dürr, K.; Lippert, R.; Schmid, M.; Küstner, B.; Schlücker, S.; Steinrück, H.-P.; Gottfried, J. M.; Ivanović-Burmazović, I. *Inorg. Chem.* **2015**, *54*, 6862−6872.

(30) Lukasczyk, T.; Flechtner, K.; Merte, L. R.; Jux, N.; Maier, F.; Gottfried, J. M.; Steinrück, H.-P. *J. Phys. Chem. C* **2007**, *111*, 3090−3098.

(31) Mack, J.; Stillman, M. J. In *The Porphyrin Handbook*; Elsevier, 2003; 43−116.

(32) Da Cruz, F.; Driaf, K.; Berthier, C.; Lameille, J.-M.; Armand, F. *Thin Solid Films* **1999**, *349*, 155−161.

(33) Lanznaster, M.; Neves, A.; Bortoluzzi, A. J.; Aires, V. V. E.; Szpoganicz, B.; Terenzi, H.; Severino, P. C.; Fuller, J. M.; Drew, S. C.; Gahan, L. R.; Hanson, G. R.; Riley, M. J.; Schenk, G. *JBIC, J. Biol. Inorg. Chem.* **2005**, *10*, 319−332.

(34) Imahori, H.; Norieda, H.; Nishimura, Y.; Yamazaki, I.; Higuchi, K.; Kato, N.; Motohiro, T.; Yamada, H.; Tamaki, K.; Arimura, M.; Sakata, Y. *J. Phys. Chem. B* **2000**, *104*, 1253−1260.

(35) Mongwaketsi, N.; Khamlich, S.; Klumperman, B.; Sparrow, R.; Maaza, M. *Phys. B* **2012**, *407*, 1615−1619.

(36) Gouterman, M.; Wagnière, G. H.; Snyder, L. C. *J. Mol. Spectrosc.* **1963**, *11*, 108−127.

(37) Qu, J.; Fredericks, P. *Spectrochim. Acta, Part A* **2000**, *56*, 1637−1644.

(38) Spiro, T. G. In *Iron Porphyrins*; Lever, A. B. P., Gray, H. B., Eds.; Addison-Wesley: Boston, MA, 1983; 89−159.

(39) Paulat, F.; Praneeth, V. K. K.; Näther, C.; Lehnert, N. *Inorg. Chem.* **2006**, *45*, 2835−2856.

(40) Burke, J. M.; Kincaid, J. R.; Spiro, T. G. *J. Am. Chem. Soc.* **1978**, *100*, 6077−6083.

(41) Hajduková-Šmídová, N.; Procházka, M.; Osada, M. *Vib. Spectrosc.* **2012**, *62*, 115−120.

(42) Praus, P.; Procházka, M.; Štěpánek, J.; Bok, J. *J. Mol. Struct.* **2001**, *565*−*566*, 129−132.

(43) Chen, D.-M.; Zhang, Y.-H.; He, T.-J.; Liu, F.-C. *Spectrochim. Acta, Part A* **2002**, *58*, 2291−2297.

(44) Burke, J. M.; Kincaid, J. R.; Peters, S.; Gagne, R. R.; Collman, J. P.; Spiro, T. G. *J. Am. Chem. Soc.* **1978**, *100*, 6083−6088.

(45) Lei, H.; Han, A.; Li, F.; Zhang, M.; Han, Y.; Du, P.; Lai, W.; Cao, R. *Phys. Chem. Chem. Phys.* **2014**, *16*, 1883−1893.

(46) Rywkin, S.; Hosten, C. M.; Lombardi, J. R.; Birke, R. L. *Langmuir* **2002**, *18*, 5869−5880.

(47) Tsai, H.-H. G.; Simpson, M. C. *J. Phys. Chem. A* **2004**, *108*, 1224−1232.

(48) Baldwin, M. J.; Ross, P. K.; Pate, J. E.; Tyeklar, Z.; Karlin, K. D.; Solomon, E. I. *J. Am. Chem. Soc.* **1991**, *113*, 8671−8679.

DOI: 10.1021/acs.inorgchem.6b01136
Inorg. Chem. XXXX, XXX, XXX−XXX

539 (49) Ferreira, L. M. C.; Grasseschi, D.; Santos, M. S. F.; Martins, P.
540 R.; Gutz, I. G. R.; Ferreira, A. M. C.; Araki, K.; Toma, H. E.; Angnes, L.
541 *Langmuir* **2015**, *31*, 4351−4360.
542 (50) Abdelhamid, H. N.; Wu, H.-F. *Anal. Bioanal. Chem.* **2016**, *408*,
543 4485.
544 (51) Chen, C.-Y.; Hinman, S. S.; Duan, J.; Cheng, Q. *Anal. Chem.*
545 **2014**, *86*, 11942−11945.
546 (52) Srinivasan, N.; Haney, C. A.; Lindsey, J. S.; Zhang, W.; Chait, B.
547 T. *J. Porphyrins Phthalocyanines* **1999**, *03*, 283−291.

DOI: 10.1021/acs.inorgchem.6b01136
Inorg. Chem. XXXX, XXX, XXX−XXX